ADVANCED MATERIALS
www.advmat.de

Unleashing the Kinetic Limitation of Co-Free Li-Rich Mn-Based Cathodes via Ionic/Electronic Dual-Regulation

Kai Wang, Youqi Chu, Zhencheng Huang, Hang Yang, Ming Yang, Yongbiao Mu, Xinhua Tan, Guanjie He, Mingjian Zhang, Lin Zeng, Biao Li,* Feng Pan,* and Jiangtao Hu**

Li-rich Mn-based oxide (LRMO) are promising cathode candidates for next-generation Li-ion batteries with combined cost-effectiveness and high specific capacity. Designing Co-free LRMO can further leverage the low cost of this class of cathodes given the capacity can be maintained. However, implementing cobalt-free LRMO cathode materials are hampered by their sluggish kinetics, resulting in low capacity and poor rate performance that underperform compared with their Co-containing counterparts. Here, it is confirmed that the slow kinetics of Co-free LRMO originates from the structural disorder caused by transition metals (TMs) migration at high voltages (above 4.5 V Vs. Li^+/Li) and consequent irreversible oxygen redox process. Aware of this, Na^+/F^- is introduced in surficial lattice to alleviate these issues, ultimately achieving improved discharge voltage (≈0.2 V above 1 C, 1 C = 0.25 A g^{-1}), exceptional cycle stability in pouch-type cell (95.1% capacity retention in 1 C after 400 cycles at 25 °C, and 80.9% capacity retention after 300 cycles in 0.5 C at 45 °C) and excellent C-rate performance (≈150 mA h g^{-1} at 5 C). The newly developed Na^+/F^- gradient design unleashes the surficial charge transfer kinetics limitation and greatly improves the lattice structure stability, consequently providing valuable guidelines for future high-capacity LRMO cathode design.

1. Introduction

The development of high-specific capacity cathode materials is essential for enhancing the energy density of lithium-ion batteries (LIBs), and thus extending the driving range of electric vehicles and enabling grid-scale energy storage.[1,2] Currently, widely used layered oxide cathodes in commercial LIBs are either $LiCoO_2$ (LCO) or Ni-rich $Li[Ni_xCo_y(Al\text{ or }Mn)_{1-x-y}]O_2$ (NCA or NCM). However, these materials face challenges such as high cost due to cobalt reserves, insufficient capacity, and poor cyclic stability at high voltage.[3–7] To address the cost issue, the Co-less/Co-free cathode systems are being widely explored recently.[8,9] Among the alternative TMs, Mn is by far the most attractive option due to its significantly lower cost compared to Co and its non-toxic nature.[10,11] Consequently, there has been a surge of interest in Mn-based layered oxides. Particularly, the LRMO with the chemical formula of $Li_{1+a}Ni_xCo_yMn_zO_2$,

K. Wang, X. Tan, F. Pan
School of Advanced Materials
Shenzhen Graduate School
Peking University
Shenzhen, Guangdong 518055, P. R. China
E-mail: panfeng@pkusz.edu.cn

Y. Chu, Y. Mu, L. Zeng
Department of Mechanical and Energy Engineering
Southern University of Science and Technology
Shenzhen, Guangdong 518055, P. R. China
E-mail: zengl3@sustech.edu.cn

Z. Huang, M. Yang, J. Hu
Graphene Composite Research Center
College of Chemistry and Environmental Engineering
Shenzhen University
Shenzhen 518060, P. R. China
E-mail: hujt@szu.edu.cn

H. Yang, G. He
Christopher Ingold Laboratory
Department of Chemistry
University College London
20 Gordon Street, London WC1H 0AJ, UK

M. Zhang
School of Science and Engineering
The Chinese University of Hong Kong
Shenzhen, Guangdong 518172, P. R. China

B. Li
Beijing Key Laboratory of Theory and Technology for Advanced Batteries Materials
School of Materials Science and Engineering
Peking University
Beijing 100871, P. R. China
E-mail: biaoli@pku.edu.cn

The ORCID identification number(s) for the author(s) of this article can be found under https://doi.org/10.1002/adma.202504642

DOI: 10.1002/adma.202504642

(x + y + z = 1-a) have garnered great attention owing to their impressive reversible specific capacity (~280 mA h g^{-1}) and excellent energy density.[12–16]

It has been discovered that the presence of Co^{3+} in Li_2MnO_3 component can enhance its electrochemical activation and promote the participation of anions in the reaction, resulting in increased capacity compared to Co-free compounds.[17] Nevertheless, Co^{3+} is more effective than Ni^{2+} in mediating the kinetics as it promotes greater migration of TMs, resulting in less cationic redox but more oxygen redox, more O_2 release, poorer cycling performance, and more severe voltage decay.[1] Hence, future design of LRMO cathode materials could be along the lines of increasing the Ni content, and decreasing the Co content, and even fully eliminating the use of Co.

The energy density of Co-free LRMO is greatly limited at higher current densities due to impeded interfacial kinetics, which restricts their application in scenarios such as fast charging devices and grid-scale energy storage.[18] The poor rate capability of LRMO generally originates from sluggish kinetics of anionic redox that constitutes more than half of the capacity. This can be inferred from the more suppressed redox capacity and more increased overpotential in monitoring the evolution of dQ/dV plots by varying the cycling rates.[19] The underlying origin of such sluggishness of anionic redox is rooted at the structural rearrangement, such as O-O dimerization, cation migration, and octahedra distortion, that largely lags behind electron transfer. The poor rate performance could be aggravated by removing Co from LRMO as Co is better than Ni in mediating the structural reorganization kinetics. Other alternative explanations also exist to explain the limited kinetics in LRMO. Previous reports have uncovered that, when Li^+ are constantly removed from the LRMO, oxygen evolution occurs to compensate for the decreased positive charge in the lattice.[20] This leads to instability of the oxygen-bonded TMs and induces a structural rearrangement, known as layered-to-spinel phase transition. Consequently, this phase transition hinders easy Li insertion and reduces capacity during subsequent discharge,[21] which is considered as the main reason for poor rate performance.[22,23] Moreover, the rapid delithiation occurring at high current densities can easily cause local structural transformations that restrict the diffusion rate of Li^+, thereby inhibiting the rate capability.[24] Conventional inert coating layer can significantly reduce the charge transfer kinetics at the interface,[25,26] while the active materials offers limited assistance in enhancing interfacial kinetics due to lattice mismatch or poor cladding uniformity.[27,28] Therefore, it is imperative to consider the design strategies during material synthesis in order to enhance the kinetics of Co-free LRMO cathodes.

Here, the typical Co-free LRMO cathodes ($Li_{1.2}Ni_{0.2}Mn_{0.6}O_2$) are tailored by introducing a trace amount of Na^+ and F^- into LRMO using a concentration gradient doping strategy to improve its kinetics. Through theoretical calculations and advanced characterizations, it can be concluded that the Na^+/F^- enriched surface inhibits the local structural transformation in high state of charges (SOCs), alleviates the TMs migration and lattice oxygen release, thus resulting in an improved recovery of discharge voltage. Moreover, the enhanced Li layer spacing through Na^+ doping and the improved electronic conductivity facilitated by F^- doping successfully compensate for the kinetic deficiencies inherent in Co-free LRMO cathodes. This results in superior rate capability, outstanding structural stability, and better kinetics due to directional element substitution, providing insights into interface engineering to unleashing the kinetic limitation in Co-free LRMO cathodes.

2. Results

2.1. Na^+ and F^- Occupation Sites Investigation

The pristine $Li_{1.2}Ni_{0.2}Mn_{0.6}O_2$ (NMPR) was obtained by oxalic acid co-precipitation, and Na^+/F^- co-doping sample $Li_{1.2-X/100}Na_{X/100}Ni_{0.2}Mn_{0.6}O_{2-X/100}F_{X/100}$ (NMCD-X, X = 1, 2, 3) was synthesized by adding stoichiometric Na^+/F^- sources into the late stage of co-precipitation (Figure S1, Supporting Information). Scanning electron microscopy (SEM) images revealed that both NMPR and NMCD-X consisted of irregular secondary particles, with a size ranging from 2 to 3 µm (Figure S2, Supporting Information). The Ni, Mn, Li, and Na contents in NMPR and NMCD-X were determined using inductively coupled plasma atomic emission spectrometry (ICP-AES) (Table S1, Supporting Information). Meanwhile, fluorine content was validated by the F ion selection electrode. (Table S2, Supporting Information). These results demonstrate that the synthesis process does not result in any loss of elements. To confirm the occupancy site of Na^+/F^- in NMCD-X, the crystal structure of NMPR and NMCD-2 were characterized by powder X-ray diffraction (XRD) (Figure S3, Supporting Information) and neutron powder diffraction (NPD) (**Figure 1**a,b). The results of joint Rietveld refinement analysis (Tables S3–S8, Supporting Information) indicate that Na^+ occupies the Li site in the alkali metal (AM) layer, while F^- replaces the O^{2-} site. The successful incorporation of Na and F is further corroborated by the increased *c*-parameter and decreased a-parameter as obtained in the refinement results (Figure S4, Supporting Information), since Na^+ has larger ionic radii than Li^+ while F^- is smaller than O^{2-}.

High-angle annular dark field scanning transmission electron microscopy (HAADF-STEM) technique was utilized to examine the local structure of NMPR and NMCD-2 (Figure S5, Supporting Information). The corresponding fast Fourier transform (FFT) patterns of the surface area reveal a distinct spinel layer (~2–3 nm thick). This layer visible at the surface of both NMPR and NMCD-2 may be attributed to the segregation of Ni^{2+}.[29] The electron energy loss spectra (EELS) mapping performed on the surface regions of NMPR and NMCD clearly reveals Ni enrichment (Figure S6, Supporting Information). By performing the inverse fast Fourier transform (IFFT) of the NMPR and NMCD-2 bulk phase regions shown in Figures S7 and S8 (Supporting Information), the interlayer spacing of the TMs layer can be expanded from 0.471 nm (NMPR) to 0.473 nm (NMCD-2) after co-doping with Na^+ and F^-. The multi-scale characterizations provide collective evidences to the increased layer spacing due to the co-doping.

Atomic contrast measurements were conducted on the AM layer, which is proportional to Z^2 (Z = atomic number).[30] The identified quantified regions are highlighted by a red rectangle in Figure 1c,d. Due to that only TMs atoms can be visualized in the HAADF image, a uniformly spaced atomic arrangement can be observed in the AM layer of NMPR, which can be attributed to the

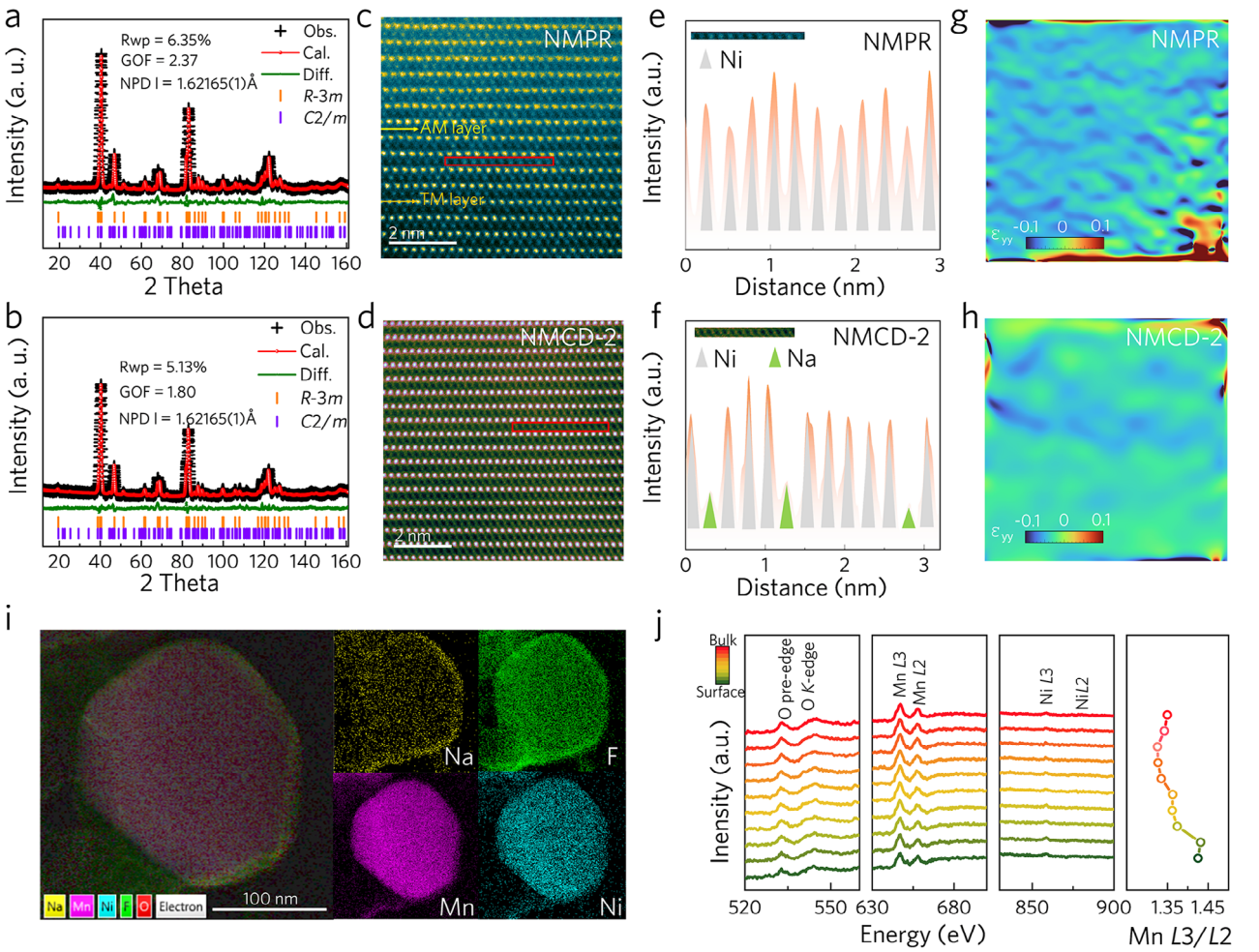

Figure 1. Atomic-level observation of NMPR and NMCD-2. a,b) NPD Rietveld refinement results, including NMPR (a) and NMCD-2 (b). c,d) HAADF-STEM images of NMPR (c) and NMCD-2 (d) at the near-surface area. e,f) Corresponding intensity profiles of selected Li slabs of NMPR (e) and NMCD-2 (f), marked by the red-line frames in (c) and (d). g,h) GPA patterns of NMPR (g) and NMCD-2 (h), deduced from the corresponding HAADF-STEM images in (c) and (d). i) The cross-section HRTEM-EDS image of NMCD-2. Scale bar: 100 nm. j) the O *K*-edge, Mn *L*-edge and Ni *L*-edge EELS spectra of NMCD-2 derived from Figure S16b (Supporting Information) and the ratio of white line of Mn *L*3/*L*2 by non-linear least squares (NLLS) analysis.

anti-occupancy of Li^+ and Ni^{2+} (Figure 1e). In NMCD-2, atomic columns within the AM layer exhibit two distinct contrast levels in the HAADF-STEM image (Figure 1f). Based on Z-contrast principles, the weaker intensity regions are attributed to Na atom columns, while the stronger features correspond to antisite Ni atoms occupying AM positions. This assignment is further corroborated by atomic contrast line scan along different direction (Figure S9, Supporting Information).

Geometric phase analysis (GPA) was conducted on atomic-resolved HADDF-STEM images of NMPR and NMCD-2 (Figure 1c,d) to investigate the effect of co-doping on stress distribution. As shown in Figure 1g,h, there is a slightly lower internal strain in NMCD-2 as compared to NMPR, which may be attributed to decreased Li/Ni mixing. Moreover, scanning transmission microscopy-energy dispersive spectroscopy (STEM-EDS) was utilized to monitor the distribution of elements in NMCD-2, revealing successful doping of Na^+ and F^- ions (Figure S10, Supporting Information). The Na^+ and F^- elements aggregate on the surface of the particles, which is confirmed by cross-section focused ion beam (FIB) (Figure 1i). Additionally, surface-sensitive and chemically selective X-ray photoelectron spectroscopy (XPS) was performed with etching to further confirm these findings. The signal of Na 1*s* (Na—O bonding energy: ~1071.27 eV)[31] F 1s (Li—F bonding energy: ~685 eV)[32] gradually weakens from the surface to the bulk phase, indicating a gradient distribution characteristic (Figures S11 and S12, Supporting Information). The stronger Mn^{3+} signals (Mn^{3+}-O binding energy: ~642.5 nm) and Ni^{2+} signals (Ni^{2+}-O binding energy: ~854.6 nm)[33] of NMCD-2 in the XPS spectra further confirm the substitution of F atoms for O atoms (Figures S13 and S14, Supporting Information) as a result of charge compensation as F^- carries less negative charges.

To illustrate the valence distribution of TMs in the two cathodes, EELS were collected. EELS of NMPR from surface to the bulk (yellow arrow) is presented in Figure S15 (Supporting Information). The ratios between *L*3 and *L*2 of Mn remain constant from surface to bulk and exceed 1.5. Concerning NMCD-2, the pre-peak of the O *K*-edge gradually increases from the surface to

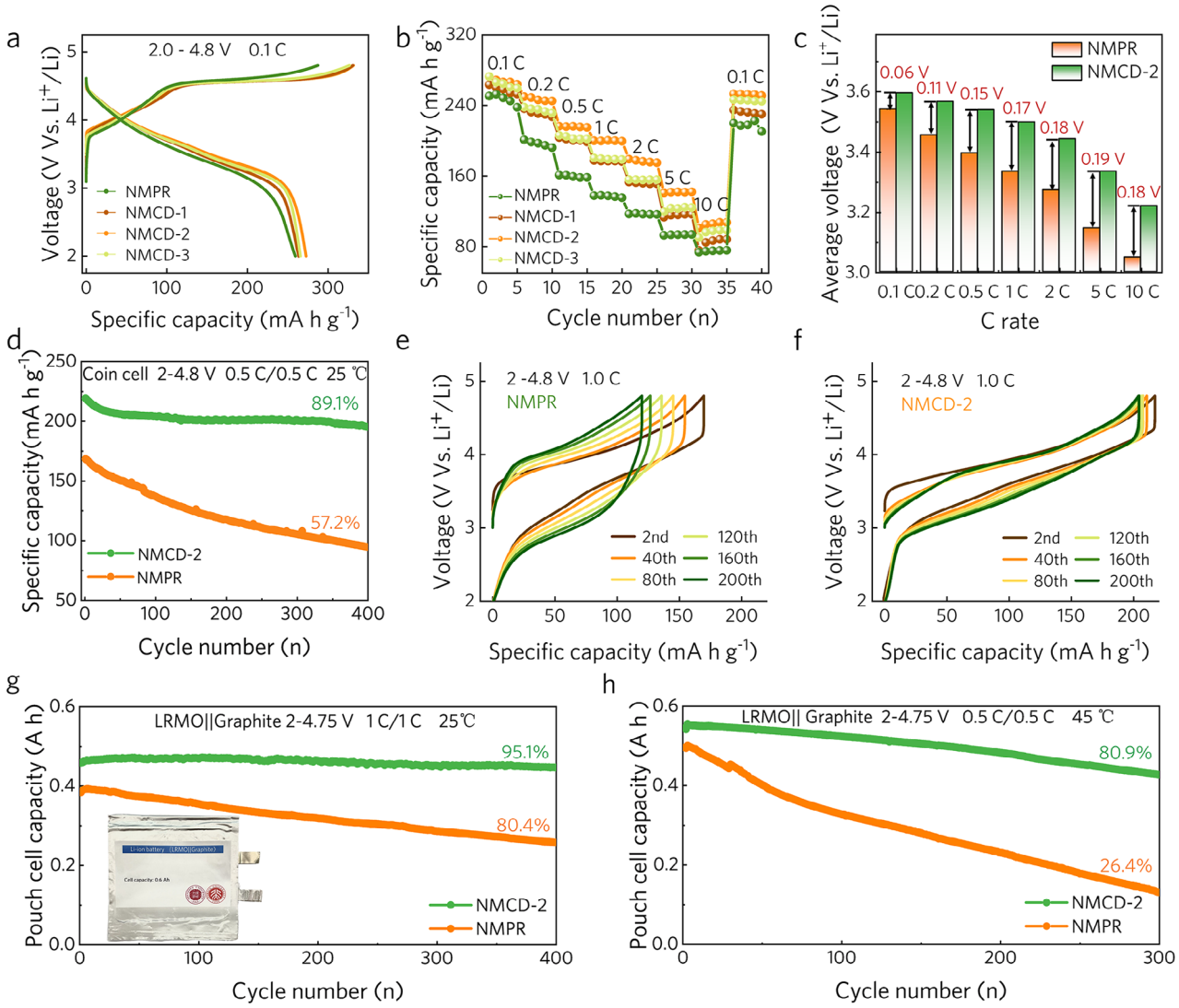

Figure 2. Electrochemical performance of NMPR and NMCD-X. a) Capacity-voltage profiles of NMPR and NMCD-X at 0.1 C. b) C-rate performance of NMPR and NMCD-X. c) Average discharge voltage at different current densities for NMPR and NMCD-2. d) Cycling stability of NMPR and NMCD-2 at 0.5 C in half cell. e,f) Selected charge–discharge curves of NMPR (e) and NMCD-2 (f) in the 200 cycles at 0.5 C. g) Pouch-type cell cycling performance of NMPR and NMCD-2 with graphite as anode at 1 C, 25 °C. h) Pouch-type cell cycling performance of NMPR and NMCD-2 with graphite as anode at 0.5 C, 45 °C.

the bulk, suggesting an increased covalency of TM—O[34] bonds (Figure 1j; Figure S16, Supporting Information). This finding is consistent with the gradient distribution characteristics of the F^- and verifies that there are more TM-F bonds on the surface. Additionally, the *L3*/*L2* ratios of Mn were quantified, which gradually decrease from the surface to the bulk with a value less than 1.5. The result indicates that NMCD-2 exhibits lower valence state of Mn elements on the surface area, due to the gradient substitution from the F^- element.[35]

2.2. Superior Cycle Performance and Improved Rate Capability

The electrochemical performance of NMCD-X and NMPR was first evaluated using Li-metal as the negative electrode in coin cells. **Figure 2a** displays the initial charge–discharge voltage curves of the prepared LRMO cathodes at 0.1 C (1 C = 250 mA g^{-1}). NMCD-X materials exhibit a longer oxygen oxidation plateau than NMPR, and larger discharge capacities overall, as well as an increase in the average discharge voltage due to Na^+/F^- doping. Among the four cathodes, NMCD-2 exhibits the highest discharge capacity (273.11 mA h g^{-1}) and discharge average voltage (3.61 V). Moreover, the NMCD-X cathodes show significantly optimized rate performance compared to NMPR, particularly NMCD-2, which retains a specific capacity of 143.9 mA h g^{-1} even at 5 C (Figure 2b). Furthermore, the cyclic voltammetry (CV) test conducted at varying scan rates indicates that NMCD-2 has a fast Li^+ diffusion rate (Figures S17,S18, and Note S1, Supporting Information). A comparison was made between the average voltages of NMPR and NMCD-2 at different

C-rates. The results indicate that NMCD-2 demonstrates an improved average discharge voltage exceeding 0.15 V as the current density increases to 0.5 C or higher (Figure 2c). NMCD-2 exhibits the best cycling performance among the NMCD-X cathodes. (Figure S19, Supporting Information). Figure 2d, Figures S20 and S21 (Supporting Information) present a comparison of the long-term cycling performance between NMPR and NMCD-2 at various current densities. After 400 cycles at 0.5 C with a cut-off voltage of 4.8 V, the capacity of NMPR decreased to 94.67 mA h g^{-1}, which corresponds to a capacity retention of 57.2% relative to its initial capacity. In contrast, NMCD-2 exhibits 89.1% capacity retention after 400 cycles. By comparing the half-cell performance of $Li_{1.2}Ni_{0.2}Mn_{0.6}O_2$ with those reported recently,[36–40] NMCD-2 shows significant superiority (Figure S22, Supporting Information). The charge–discharge curves of NMPR and NMCD-2 were compared during the initial 200 cycles at 0.5 C, as illustrated in Figure 2e,f. The results showed that NMCD-2 effectively suppressed voltage and capacity attenuation. Furthermore, the dQ/dV curves of NMPR and NMCD-X were also plotted and compared, indicating that NMCD-2 exhibited minimal voltage decay during the first 400 cycles at 0.5 C and 4 C (Figures S23 and S24, Supporting Information). CV tests of NMPR and NMCD-2 after 2 and 200 cycles at 0.5 C were also performed (Figure S25, Supporting Information). For NMPR, the reduction peak for $Ni^{2+/3+/4+}$ shifted significantly towards lower potentials, and a distinct reduction peak linked to spinel (at ≈2.8 V) appeared in the discharge curve after two cycles. In contrast, NMCD-2 showed an almost unchanged reduction peak with no visible spinel peak, demonstrating its remarkable structural stability during cycling. The long-term cycling performance of NMPR and NMCD-2 was analyzed at 4.0 C. NMCD-2 exhibited superior performance, retaining 91.2% of its capacity after 1000 cycles, compared to 80.4% of its capacity of NMPR after the same cycles (Figure S26, Supporting Information). Notably, NMCD-2 exhibited a voltage decay rate of merely 0.72 mV per cycle, significantly lower than the 0.94 mV per cycle observed in NMPR. Additionally, NMCD-2 shows a discharge capacity that exceeds the NMPR by over 50 mA h g^{-1} at 4 C, accompanied by more symmetrical charge and discharge curves (Figure S27, Supporting Information).

NMPR and NMCD-2 were further evaluated in a full cell configuration, with graphite as the anode, in a 0.6 A h pouch-type cell (Figure 2g). Specific details of the pouch-type cell parameters can be found in Table S9 (Supporting Information). Notably, NMCD-2 presented minimal capacity decay in the 400 cycles at 1 C (95.1%), surpassing that of NMPR (80.4%). Our NMCD-2 sample exhibited the top level in terms of capacity retention compared to recently reports at room temperature, both in half cells and pouch cells (Figure S28 and Table S10, Supporting Information). The high-temperature cycling performance of the two cathodes at 45 °C in pouch-type cells were also assessed (Figure 2h), and NMCD-2 cell maintained at a practical level of reversible cycling (80.9% retention after 300 cycles in 0.5 C), while NMPR only retained 26.4%.

As demonstrated in Figure S29 and Note S2 (Supporting Information), the surface Na^+ retained after cycling exhibits dual stability: it neither participates in Li^+ extraction processes nor migrates into the vacancies within the TM layer. This inherent stability effectively mitigates lattice distortion and consequently prevents material degradation through structural collapse.

2.3. Redox Processes and Structural Change

Operando Differential Electrochemical Mass Spectrometry (DEMS) was performed to detect the gas evolution in the coin cells with NMPR and NMCD-2 as the cathode, respectively. The results demonstrated that O2 generation was roughly three times higher in NMPR compared to NMCD-2. The NMCD-2 electrode releases oxygen at 4.51 V during the first charge, but it is 4.48 V in the NMPR, implying greater stability of lattice oxygen in NMCD-2.[41] (**Figure 3**a,b). In addition, TMs dissolution was confirmed by in situ Ultraviolet-Visual (UV–vis) spectra, which were obtained from an assembled cuvette cell (Figure S30 and Note S3, Supporting Information). UV–vis absorption spectra of NMPR and NMCD-2 were collected at different SOCs during the initial cycle. The broad peak associated with TMs dissolution was observed within the range of 380–430 nm.[42] To amplify the changes, the data underwent first-order differential processing. As depicted in Figure 3c,d, NMCD-2 exhibited a significantly less TMs dissolution signal during the initial cycle. Reduced dissolution of TMs reflects fewer interfacial side reactions and phase transitions at the surface.[43]

The in situ galvanostatic electrochemical impedance spectroscopy (GEIS) measurements, with distribution of relaxation time (DRT) analysis, tracked the impedance evolution of NMPR and NMCD-2 at different SOCs in the initial cycle. The peaks observed in the range of 10^{-1} to 10^{2} s are attributed to the charge transfer impedance (R_{ct}) at the cathode/electrolyte interface (CEI), and the peaks ranging from 10^{-3} to 10^{-2} s are attributed to the impedance of CEI (R_{CEI}).[44] As shown in Figure 3e, the impedance varies with the SOCs mostly in the low and mid-frequency ranges. As the cell is charged from the open-circuit voltage (OCV) to 4.8 V (Vs. Li^+/Li), the R_{ct} increases from ≈250 to 2000 Ω in NMPR. By contrast, NMCD-2 displays only minor modifications in impedance in the low-frequency area. Meanwhile, its R_{ct} increases from 20 to 720 Ω throughout charging, which is far below the variation observed in NMPR (Figure 3f). This result indicates that the interfacial diffusion kinetics of NMCD-2 cathode is more rapid than those of NMPR. The corresponding Nyquist plots and electrochemical curves are illustrated in Figures S31 and S32 (Supporting Information).

To gain deeper insight into the structural transformations induced by Na^+/F^- doping and their impact on the structural robustness of this material during the cycling process, in situ XRD was measured. As shown in Figure 3g,h, in situ XRD data were collected on NMPR at 0.3 C in initial cycle (3–4.8 V Vs. Li^+/Li). The lattice parameter refinement was carried out using the (003) and (101) peaks with a space group of *R*-3*m*. During the charging process, the *c*-axis increases while the *a*-axis shrinks due to the oxidation of the TMs, and the opposite tendency occurs during the discharging process. NMCD-2 shows a flatter *c*-axis change in plateau region, implying a smaller local structural changes during oxygen redox reactions (Figure 3h).[16] The improved structure stability of NMCD-2 enabled by the presence of Na^+ and F^- was further validated by the *c*-axis expansion value during the

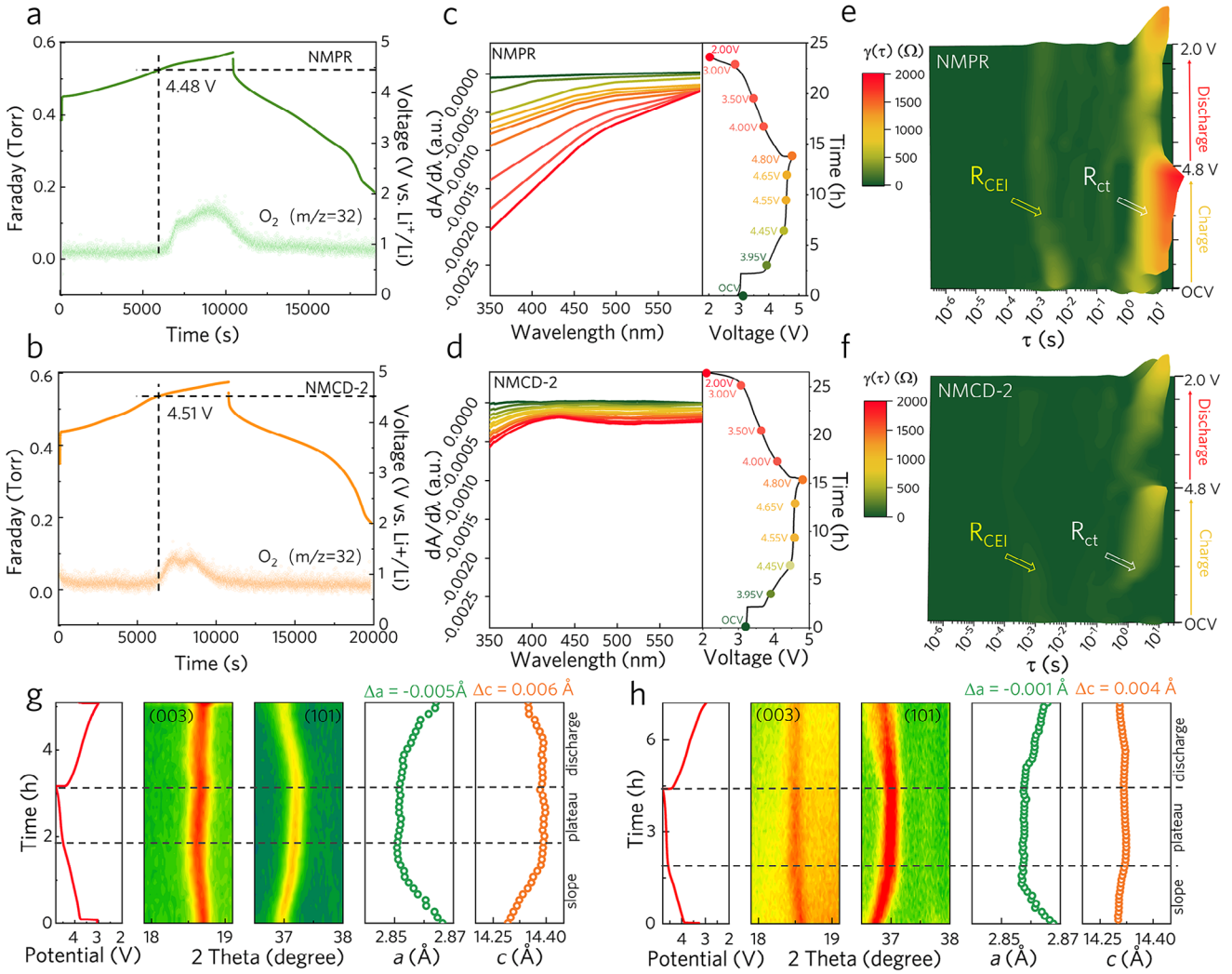

Figure 3. In situ characterizations in the initial cycle. a,b) The result of gas evolution during the first cycle of NMPR (a) and NMCD-2 (b). c,d) In situ UV–vis absorption spectroscopy at different SOCs during the initial cycle of NMPR (c) and NMCD-2 (d) and corresponding electrochemistry curves. e, f, DRT analysis transformed from GEIS of NMPR (e) and NMCD-2 (f) during the initial cycle. g,h) In situ XRD spectra and the corresponding Rietveld refinement results of NMPR (g) and NMCD-2 (h).

first cycle, which was 0.004 Å, lower than that in the NMPR cathode (0.006 Å).[45]

2.4. TM—O and TM-TM Bonds Evolution

The normalized X-ray absorption near edge structure (XANES) was used to analyze TMs (Ni, Mn) at various SOCs, including OCV, a fully charged state of 4.8 V (Ch-4.8 V), and a fully discharged state of 2 V (Disch-2 V), in order to explore the effect of Na^+/F^- doping on TMs redox reactions, local coordination environments, and oxygen redox (**Figure** 4a–d). It is evident that the Mn and Ni K-edge of NMCD-2 at OCV and discharge states well superimpose together, indicating excellent reversibility and effective suppression of Mn^{2+}/Mn^{3+}.[46] Figure 4e–h shows the fitted extended X-ray absorption fine structure (EXAFS) for each TM element in the first cycle. Compared to NMPR, NMCD-2 effectively restored the local order of both TM—O and TM-TM after the first cycle. The significant minimization of TM—O and TM-TM coordination environment changes in NMCD-2 suggests that Na^+/F^- substitution effectively reduces the irreversible migration of TMs and enhances the lattice oxygen stability.

The EXAFS data was fitted to analyze the chemical bond length and Debye-Waller factors (Note S4, Supporting Information). It is evident that the doping of Na^+/F^- considerably lessens the alteration of the TM—O and TM—TM bond length. In addition, the variability of bond length is more reversible in NMCD-2, notably for Ni (Figure 4i–l). The Debye-Waller factor of σ^2_{Mn-O} shows a slight increase during the initial cycle in NMCD-2 (Figure S33a and Table S11, Supporting Information). This results in the prevention of elevation of oxygen release and angular distortion of TM—O ordering. σ^2_{Mn-TM}, σ^2_{Ni-O}, and σ^2_{Ni-TM} increased during the charging, but partially recovered during discharging, indicating a more reversible TMs migration in NMCD-2

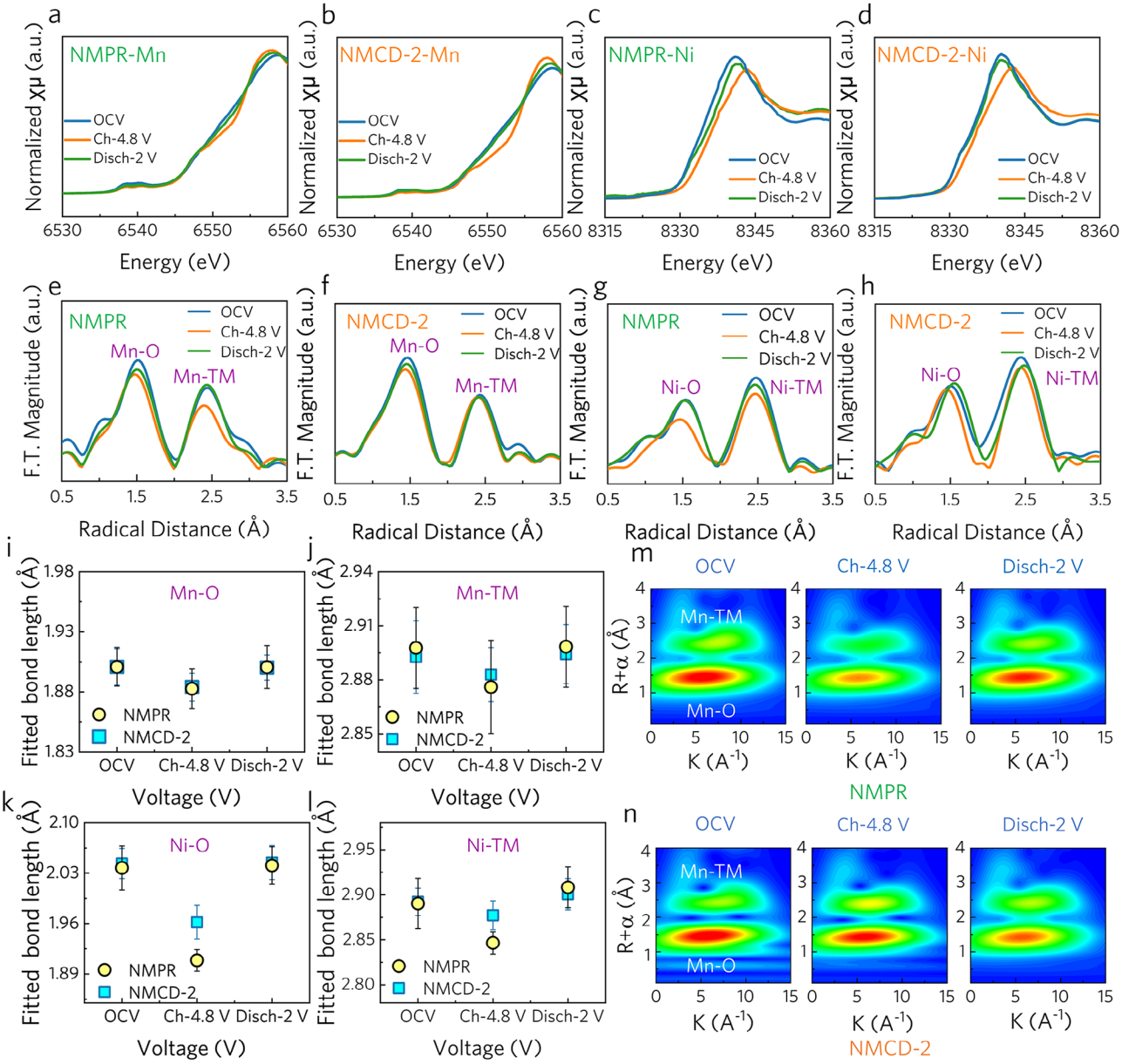

Figure 4. X-ray absorption spectroscopy analysis of NMPR and NMCD-2. a–d) Fitted Mn and Ni *K*-edge XANES spectra of NMPR and NMCD-2 at OCV (blue), Ch-4.8 V (orange), and Disch-2.0 V (green), respectively. e–h) Fitted Mn and Ni EXAFS spectra of NMPR and NMCD-2 at OCV (blue), Ch-4.8 V (orange), and Disch-2.0 V (green), respectively. i–l) Change of Mn—O (i), Mn—TM (j), Ni—O (k) and Ni—TM (l) bond length during the activation process of NMPR and NMCD-2 based the fitting by Artemis (based on *R*-3*m* space group). m,n) WT fitting results of Mn EXAFS spectra at different SOCs of NMPR (m) and NMCD-2 (n) based on *R*-3*m* space group.

(Figures S33b,S34, and Table S12, Supporting Information). Figure 4m,n and Figure S35 (Supporting Information) depict the results of the wavelet transforms (WT) fitting of Mn and Ni EXAFS spectra, which confirm the involvement of Na^+/F^- doping in the reversible migration of TMs and oxygen redox in initial cycle.

High-resolution transmission electron microscopy (HRTEM) images of the post-cycled NMPR and NMCD-2 were performed (Figures S36 and S37, Supporting Information). The surface of NMPR and NMCD-2 remained in a layered structure after the first cycle. However, after 400 cycles, a distinct surface reconstruction from layered to Rock-salt was noticed in NMPR, while NMCD-2 maintained its primary layered structure with only a ~10 nm Spinel layer being detected. The main peaks in the XRD patterns of the cycled NMPR cathode exhibit a significant decrease in intensity and broadening upon cycling, whereas the corresponding peaks in NMCD-2 remain sharp and intense, indicating the excellent crystallinity and structural integrity (Figure S38, Supporting Information). As shown in Figure S39 (Supporting Information), the resistance data of NMPR and NMCD-2 further confirms the observed phase change captured by the HRTEM images.

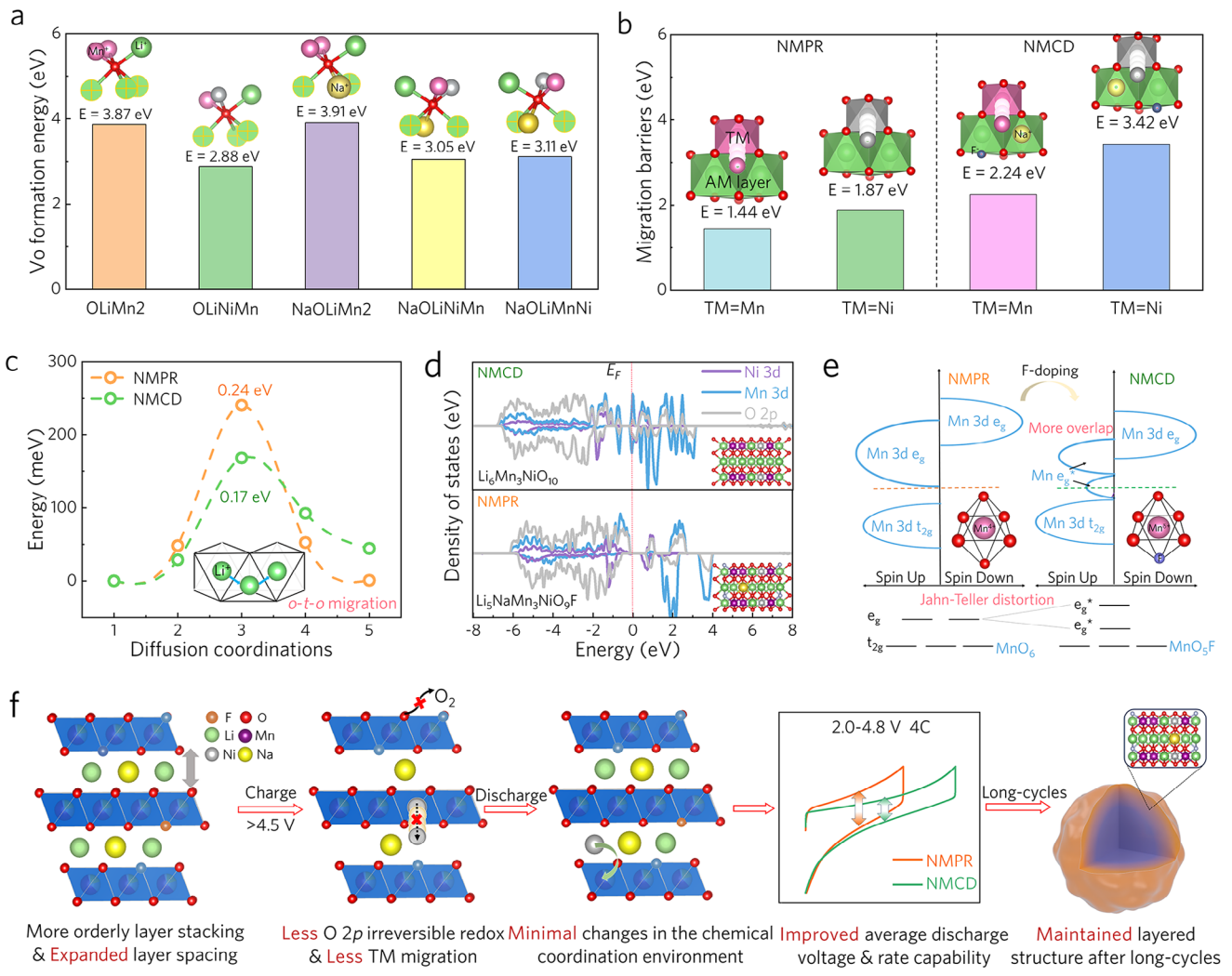

Figure 5. Theoretical Calculations and Schematic Illustration of Kinetics Enhancement. a) The V_o formation energies in the Li-O-Li configuration of NMPR and NMCD. b) The migration energy barriers of TM ions along the *c*-axis in NMPR and NMCD. c) The energy barrier of the *o-t-o* migration path in AM layer in NMPR and NMCD. d) The pDOS curves of $Li_6Mn_3NiO_{10}$ and $Li_5NaMn_3NiO_9F$. e) Schematic pDOS of $Li_6Mn_3NiO_{10}$ and $Li_5NaMn_3NiO_9F$. f) Schematic diagram of the mechanism of role of Na^+/F^- in suppressing voltage hysteresis and maintaining the stability of the structure.

2.5. First-Principles Calculations

The effect of Na^+/F^- substitution on oxygen vacancies (V_o) and TMs migration was investigated using first-principles calculations to elucidate the observed discrepancy in kinetic improvements. It is known that the occupation of Li^+ in the TMs layer changes the local electron distribution of O and forms a Li-O-Li configuration. Since Li^+ is weakly bonded to the neighboring O 2*p*, the lattice O^{2-} is more prone to lose electrons at high voltages, thereby inducing the anion redox reaction and irreversible local structural transitions.[47] Hence, the formation energy of V_o is an indicator of the structural stability of the LMRO. The V_o at different sites in the NMPR and NMCD lattice in the delithiation state were evaluated (V_o are preferentially generated in Li-O-Li configuration in delithiation state),[48] and their corresponding formation energies are 3.87 eV (OLiMn2), 2.88 eV (OLiNiMn), 3.91 eV (NaOLiMn2), 3.05 eV (NaOLiNiMn), and 3.11 eV (NaOLiMnNi), respectively (Figure S40 and Note S5, Supporting Information). It is clear that the introduction of Na^+/F^- hinders the formation of V_o in the Li-O-Li configuration by enhancing O 2*p* bonding, resulting in the stabilization of the lattice oxygen.

To further investigate the effect of Na^+/F^- substitution on the migration of TMs, the migration barriers of Ni and Mn along the *c*-axis from the TMs layer to the Li layer (tetrahedral site) were calculated by first-principles nudged-elastic band (NEB) methods (Figure S41, Supporting Information). The migration barriers of Mn in NMPR and NMCD are 1.44 and 2.24 eV, and the migration barriers of Ni in NMPR and NMCD are 1.87 and 3.42 eV, respectively (**Figure 5b**). This indicates that the migration of TMs in NMCD is considerably more challenging compared to that in NMPR. Hence, the limited TMs migration into the Li layer contributes to the maintenance of a stable crystal structure and the reversible oxygen redox reaction.

The Li^+ diffusion kinetics in the AM layer was also evaluated by the NEB calculations. The Li^+ transport follows a tetrahedral site hopping (TSH) mechanism,[49] wherein the Li^+ hops from one

octahedral site to another through an intermediate tetrahedral site (*o-t-o*).[24] The migration barrier of Li^+ during the *o-t-o* transfer decreases from 0.24 eV in NMPR ($Li_xMn_3NiO_{10}$) to 0.17 eV in NMCD ($Li_{x-1}NaMn_3NiO_9F$) (Figure 5c; Figure S42, Supporting Information), which is conducive to increasing the rate performance. As shown in Figure S43 (Supporting Information), the diffusion barrier for Na^+ within the alkali metal layer is calculated to be 0.42 eV, significantly higher than that of Li^+ (0.17 eV). This stark contrast in energy barriers explicitly confirms the preferential deintercalation of Li^+ over Na^+ during electrochemical cycling. Moreover, density of states (DOS) calculations indicate that F doping results in an increased DOS at the Fermi energy level for Li_2MnO_3-like structural units (Figure 5d). This increase in DOS enhances the electrical conductivity of NMCD, leading to a further increase on the rate capability.[50] The enhanced conductivity can be attributed to the symmetry breaking of MnO_6 caused by F doping, which introduces the Jahn-Teller effect. As a result, one of the orbitals moves below the Fermi energy level to maintain energy conservation (Figure 5e). Consequently, there is a reduction in bandgap and an enhancement in electronic conductivity.[51]

3. Conclusion

By employing in situ characterization and calculations, we have successfully confirmed that the sluggish kinetics in $Li_{1.2}Ni_{0.2}Mn_{0.6}O_2$ primarily stem from the structure transformations occurring at high SOCs, as demonstrated in Figure 5f. The introduction of Na^+ and F^- ions effectively suppresses the migration of TMs while enhancing the bonding of O 2*p*, thereby significantly mitigating phase transitions at high SOCs and consequently improving interfacial kinetics. Furthermore, co-doping with Na^+/F^- significantly enhances both ionic and electronic conductivities in LRMO cathode, leading to a remarkable enhancement in rate capability and exceptional cycle stability. As demonstrated here, we have successfully prepared stable and high power Co-free LRMO cathodes through gradient co-doping of Na^+/F^-, which were tested in LRMO||Graphite pouch-type cells, exhibiting 95.1% capacity retention at 1 C after 400 cycles at 25 °C and 80.9% retention after 300 cycles at 0.5 C at 45 °C. These findings offer promising prospects for the application of Co-free LRMO materials in future industries such as grid-scale energy storage and electric vehicles.

Supporting Information

Supporting Information is available from the Wiley Online Library or from the author.

Acknowledgements

K.W. and Y.C. contributed equally to this work. The authors are grateful for the financial support of Basic and Applied Basic Research Foundation of Guangdong Province (No. 2021B1515130002), Shenzhen Science and Technology Program (No. KJZD20230923115005009), Soft Science Research Project of Guangdong Province (No. 2017B030301013), the National Natural Science Foundation (NNSF) of China (No. 52202269). This work was also financially supported by the Stable Support Plan Program for Higher Education Institutions (20220815094504001).

Conflict of Interest

The authors declare no conflict of interest.

Data Availability Statement

The data that support the findings of this study are available from the corresponding author upon reasonable request.

Keywords

gradient doping, high electrochemical performance, ionic/eletronic regulation, Li-rich Co-free cathode

Received: March 8, 2025
Revised: April 30, 2025
Published online:

[1] B. Li, Z. Zhuo, L. Zhang, A. Iadecola, X. Gao, J. Guo, W. Yang, A. V. Morozov, A. M. Abakumov, J.-M. Tarascon, *Nat. Mater.* **2023**, *22*, 1370.
[2] B. Li, K. Zhang, Y. Yang, Y. Zuo, X. Li, D. Xia, *Adv. Mater.* **2024**, *36*, 2400259.
[3] J. Li, C. Lin, M. Weng, Y. Qiu, P. Chen, K. Yang, W. Huang, Y. Hong, J. Li, M. Zhang, C. Dong, W. Zhao, Z. Xu, X. Wang, K. Xu, J. Sun, F. Pan, *Nat. Nanotechnol.* **2021**, *16*, 599.
[4] J.-N. Zhang, Q. Li, C. Ouyang, X. Yu, M. Ge, X. Huang, E. Hu, C. Ma, S. Li, R. Xiao, W. Yang, Y. Chu, Y. Liu, H. Yu, X.-Q. Yang, X. Huang, L. Chen, H. Li, *Nat. Energy* **2019**, *4*, 594.
[5] C. Xu, K. Märker, J. Lee, A. Mahadevegowda, P. J. Reeves, S. J. Day, M. F. Groh, S. P. Emge, C. Ducati, B. L. Mehdi, C. C. Tang, C. P. Grey, *Nat. Mater.* **2021**, *20*, 84.
[6] Y. Bi, J. Tao, Y. Wu, L. Li, Y. Xu, E. Hu, B. Wu, J. Hu, C. Wang, J.-G. Zhang, Y. Qi, J. Xiao, *Science* **2020**, *370*, 1313.
[7] W. Huang, C. Lin, J. Qiu, S. Li, Z. Chen, H. Chen, W. Zhao, G. Ren, X. Li, M. Zhang, F. Pan, *Chem* **2022**, *8*, 2163.
[8] J. U. Choi, N. Voronina, Y.-K. Sun, S.-T. Myung, *Adv. Energy Mater.* **2020**, *10*, 2002027.
[9] U.-H. Kim, G.-T. Park, B.-K. Son, G. W. Nam, J. Liu, L.-Y. Kuo, P. Kaghazchi, C. S. Yoon, Y.-K. Sun, *Nat. Energy* **2020**, *5*, 860.
[10] W. Huang, C. Lin, M. Zhang, S. Li, Z. Chen, W. Zhao, C. Zhu, Q. Zhao, H. Chen, F. Pan, *Adv. Energy Mater.* **2021**, *11*, 2102646.
[11] B. Ammundsen, J. Paulsen, *Adv. Mater.* **2001**, *13*, 943.
[12] P. K. Nayak, E. M. Erickson, F. Schipper, T. R. Penki, N. Munichandraiah, P. Adelhelm, H. Sclar, F. Amalraj, B. Markovsky, D. Aurbach, *Adv. Energy Mater.* **2018**, *8*, 1702397.
[13] E. Hu, X. Yu, R. Lin, X. Bi, J. Lu, S. Bak, K.-W. Nam, H. L. Xin, C. Jaye, D. A. Fischer, K. Amine, X.-Q. Yang, *Nat. Energy* **2018**, *3*, 690.
[14] J. Wang, X. He, E. Paillard, N. Laszczynski, J. Li, S. Passerini, *Adv. Energy Mater.* **2016**, *6*, 1600906.
[15] S. Hy, H. Liu, M. Zhang, D. Qian, B.-J. Hwang, Y. S. Meng, *Energy Environ. Sci.* **2016**, *9*, 1931.
[16] W. Zuo, M. Luo, X. Liu, J. Wu, H. Liu, J. Li, M. Winter, R. Fu, W. Yang, Y. Yang, *Energy Environ. Sci.* **2020**, *13*, 4450.
[17] B. Yuan, S. X. Liao, Y. Xin, Y. J. Zhong, X. X. Shi, L. Y. Li, X. D. Guo, *RSC Adv.* **2015**, *5*, 2947.
[18] Y.-X. Yao, X. Chen, N. Yao, J.-H. Gao, G. Xu, J.-F. Ding, C.-L. Song, W.-L. Cai, C. Yan, Q. Zhang, *Angew. Chem., Int. Ed.* **2023**, *62*, 202214828.
[19] B. Li, K. Kumar, I. Roy, A. V. Morozov, O. V. Emelyanova, L. Zhang, T. Koc, S. Belin, J. Cabana, R. Dedryvère, A. M. Abakumov, J.-M. Tarascon, *Nat. Mater.* **2022**, *21*, 1165.

[20] H. Zhao, W.-Y. A. Lam, L. Sheng, L. Wang, P. Bai, Y. Yang, D. Ren, H. Xu, X. He, *Adv. Energy Mater.* **2022**, *12*, 2103894.
[21] J. Rana, M. Stan, R. Kloepsch, J. Li, G. Schumacher, E. Welter, I. Zizak, J. Banhart, M. Winter, *Adv. Energy Mater.* **2014**, *4*, 1300998.
[22] J. R. Croy, K. G. Gallagher, M. Balasubramanian, B. R. Long, M. M. Thackeray, *J. Electrochem. Soc.* **2014**, *161*, A318.
[23] J. R. Croy, K. G. Gallagher, M. Balasubramanian, Z. H. Chen, Y. Ren, D. Kim, S. H. Kang, D. W. Dees, M. M. Thackeray, *J. Phys. Chem. C* **2013**, *117*, 6525.
[24] X. He, J. Wu, Z. Zhu, H. Liu, N. Li, D. Zhou, X. Hou, J. Wang, H. Zhang, D. Bresser, Y. Fu, M. J. Crafton, B. D. McCloskey, Y. Chen, K. An, P. Liu, A. Jain, J. Li, W. Yang, Y. Yang, M. Winter, R. Kostecki, *Energy Environ. Sci.* **2022**, *15*, 4137.
[25] P. Yan, J. Zheng, J. Liu, B. Wang, X. Cheng, Y. Zhang, X. Sun, C. Wang, J.-G. Zhang, *Nat. Energy* **2018**, *3*, 600.
[26] Y. Zhao, K. Zheng, X. Sun, *Joule* **2018**, *2*, 2583.
[27] U. Nisar, N. Muralidharan, R. Essehli, R. Amin, I. Belharouak, *Energy Storage Mater.* **2021**, *38*, 309.
[28] X. Zhu, T. U. Schülli, X. Yang, T. Lin, Y. Hu, N. Cheng, H. Fujii, K. Ozawa, B. Cowie, Q. Gu, S. Zhou, Z. Cheng, Y. Du, L. Wang, *Nat. Commun.* **2022**, *13*, 1565.
[29] E. Boivin, N. Guerrini, R. A. House, J. G. Lozano, L. Jin, G. J. Rees, J. W. Somerville, C. Kuss, M. R. Roberts, P. G. Bruce, *Adv. Funct. Mater.* **2021**, *31*, 2107652.
[30] N. D. Browning, M. F. Chisholm, S. J. Pennycook, *Nature* **1993**, *366*, 143.
[31] Z. Song, G. Zhang, X. Deng, K. Zou, X. Xiao, R. Momen, A. Massoudi, W. Deng, J. Hu, H. Hou, G. Zou, X. Ji, *Nano-Micro Lett.* **2022**, *14*, 64.
[32] Y. Wang, Y. Zhao, S. Zhang, L. Shang, Y. Ni, Y. Lu, Y. Li, Z. Yan, Z. Miao, J. Chen, *Angew. Chem., Int. Ed.* **2024**, *63*, 202412108.
[33] C. Cheng, M. Ding, T. Yan, J. Jiang, J. Mao, X. Feng, T.-S. Chan, N. Li, L. Zhang, *Small Methods* **2022**, *6*, 2101524.
[34] K. Luo, M. R. Roberts, R. Hao, N. Guerrini, D. M. Pickup, Y.-S. Liu, K. Edström, J. H. Guo, A. V. Chadwick, L. C. Duda, P. G. Bruce, *Nat. Chem.* **2016**, *8*, 684.
[35] F. Gong, S. Ye, M. Liu, J. Zhang, L. Gong, G. Zeng, E. Meng, P. Su, K. Xie, Y. Zhang, J. Liu, *Nano Energy* **2020**, *78*, 105284.
[36] W. Jiang, C. Zhang, Y. Feng, B. Wei, L. Chen, R. Zhang, D. G. Ivey, P. Wang, W. Wei, *Energy Storage Mater.* **2020**, *32*, 37.
[37] Y. Fan, E. Olsson, G. Liang, Z. Wang, A. M. D'Angelo, B. Johannessen, L. Thomsen, B. Cowie, J. Li, F. Zhang, Y. Zhao, W. K. Pang, Q. Cai, Z. Guo, *Angew. Chem., Int. Ed.* **2023**, *62*, 202213806.
[38] C.-J. Huang, B. Thirumalraj, H.-C. Tao, K. N. Shitaw, H. Sutiono, T. T. Hagos, T. T. Beyene, L.-M. Kuo, C.-C. Wang, S.-H. Wu, W.-N. Su, B. J. Hwang, *Nat. Commun.* **2021**, *12*, 1452.
[39] F. Wu, G.-T. Kim, T. Diemant, M. Kuenzel, A. R. Schür, X. Gao, B. Qin, D. Alwast, Z. Jusys, R. J. Behm, D. Geiger, U. Kaiser, S. Passerini, *Adv. Energy Mater.* **2020**, *10*, 2001830.
[40] F. Cao, W. Zeng, J. Zhu, J. Xiao, Z. Li, M. Li, R. Qin, T. Wang, J. Chen, X. Yi, J. Wang, S. Mu, *Small* **2022**, *18*, 2200713.
[41] K. Wang, J. Qiu, F. Hou, M. Yang, K. Nie, J. Wang, Y. Hou, W. Huang, W. Zhao, P. Zhang, J. Lin, J. Hu, F. Pan, M. Zhang, *Adv. Energy Mater.* **2023**, *13*, 2301216.
[42] J. C. Zhang, F. Y. Cheng, S. L. Chou, J. L. Wang, L. Gu, H. Wang, H. Yoshikawa, Y. Lu, J. Chen, *Adv. Mater.* **2019**, *31*, 1901808.
[43] L. Rynearson, C. Antolini, C. Jayawardana, M. Yeddala, D. Hayes, B. L. Lucht, *Angew. Chem., Int. Ed.* **2024**, *63*, 202317109.
[44] S. Sun, C.-Z. Zhao, H. Yuan, Z.-H. Fu, X. Chen, Y. Lu, Y.-F. Li, J.-K. Hu, J. Dong, J.-Q. Huang, M. Ouyang, Q. Zhang, *Sci. Adv.* **2022**, *8*, add5189.
[45] Z. Lu, J. R. Dahn, *J. Electrochem. Soc.* **2002**, *149*, A815.
[46] P. Vanaphuti, J. M. Bai, L. Ma, S. Ehrlich, K. Kisslinger, F. Wang, Y. Wang, *Energy Storage Mater.* **2020**, *31*, 459.
[47] K. Luo, M. R. Roberts, R. Hao, N. Guerrini, D. M. Pickup, Y.-S. Liu, K. Edström, J. Guo, A. V. Chadwick, L. C. Duda, P. G. Bruce, *Nat. Chem.* **2016**, *8*, 684.
[48] X. Tan, Y. Zhang, S. Xu, P. Yang, T. Liu, D. Mao, J. Qiu, Z. Chen, Z. Lu, F. Pan, W. Chu, *Adv. Energy Mater.* **2023**, *13*, 2300147.
[49] Y. Su, Q. Zhang, L. Chen, L. Bao, Y. Lu, S. Chen, F. Wu, *J. Energy Chem.* **2022**, *65*, 236.
[50] D. Ma, Z. Zhao, Y. Wang, X. Yang, M. Yang, Y. Chen, J. Zhu, H. Mi, P. Zhang, *Adv. Mater.* **2023**, *36*, 2310336.
[51] Z. Y. Lun, B. Ouyang, D. A. Kitchaev, R. J. Clement, J. K. Papp, M. Balasubramanian, Y. S. Tian, T. Lei, T. Shi, B. D. McCloskey, J. Lee, G. Ceder, *Adv. Energy Mater.* **2019**, *9*, 1802959.

